Article

Ultrathin damage-tolerant flexible metal interconnects reinforced by in-situ graphene synthesis

Check for updates

Kaihao Zhang [1,2,3,5], Mitisha Surana [4,5], Jad Yaacoub[1] & Sameh Tawfick [1] ✉

Conductive patterned metal films bonded to compliant elastomeric substrates form meshes which enable flexible electronic interconnects for various applications. However, while bottom-up deposition of thin films by sputtering or growth is well-developed for rigid electronics, maintaining good electrical conductivity in sub-micron thin metal films upon large deformations or cyclic loading remains a significant challenge. Here, we propose a strategy to improve the electromechanical performance of nanometer-thin palladium films by in-situ synthesis of a conformal graphene coating using chemical vapor deposition (CVD). The uniform graphene coverage improves the thin film's damage tolerance, electro-mechanical fatigue, and fracture toughness owing to the high stiffness of graphene and the conformal CVD-grown graphene-metal interface. Graphene-coated Pd thin film interconnects exhibit stable increase in electrical resistance even when strained beyond 60% and longer fatigue life up to a strain range of 20%. The effect of graphene is more significant for thinner films of < 300 nm, particularly at high strains. The experimental observations are well described by the thin film electro-fragmentation model and the Coffin-Manson relationship. These findings demonstrate the potential of CVD-grown graphene nanocomposite materials in improving the damage tolerance and electromechanical robustness of flexible electronics. The proposed approach offers opportunities for the development of reliable and high-performance ultra-conformable flexible electronic devices.

The 2D patterning of ultrathin metallic electrodes and interconnects bonded on a compliant polymer substrate enables their flexibility and their use in current flexible electronics such as flexible displays, wearable human health monitoring devices, and soft robot sensors[1–3]. These metal films have thicknesses ranging from hundreds of nanometers to up to a few microns and are pre-designed with 3D wrinkles or 2D serpentine-shaped structures, which can effectively lower the flexural rigidity (~thickness[3]) and minimize strains in the metal layer. This geometric feature accommodates large deformation without excessive stress concentration[4–6]. Accordingly, there have been extensive studies in the past decades focused on the design and fabrication of stretchable structures - wrinkled, noncoplanar, or serpentine - to improve the fracture resistance of flexible electronics and guarantee the electrical conductivity of thin film metal interconnects under strains. The elastomeric polymer substrate provides an elastic restoring force to the stretchable structures and supports the electronic materials to conform to the target surfaces[1,7]. Previous studies showed that strong adhesion between the metal films and the underlying elastomers could retard strain localization in metal when the stack is stretched and hence imparts enhanced ductility[8–10]. Under certain conditions, this substrate constraint can delay the crack formation and leads to over 50–60% elongation of metal films without loss of electrical conductivity[8].

Despite these advances in design, it is still challenging to prevent mechanical degradation and cracking in ultrathin metal films with large or repeated deformations. Such nanometer thin films are desirable for ultra-conformable electronics. This leads to eventual loss of electrical conductivity in real-world applications where such mechanical loadings are common. The mechanical performance of thin films, 2D and 3D patterns made by thin film deposition such as sputtering or e-beam evaporation suffers from a brittle, low toughness response. This is believed to be related to the lack of large yielding, i.e., extended dislocation activity ahead of a small crack.

[1]University of Illinois Urbana Champaign, Mechanical Science and Engineering, Champaign, IL 61801, USA. [2]The Hong Kong University of Science and Technology (Guangzhou), Smart Manufacturing Thrust, Nansha, Guangzhou, 511453 Guangdong, China. [3]The Hong Kong University of Science and Technology, Mechanical and Aerospace Engineering, Sai Kung, Hong Kong SAR, China. [4]University of Illinois Urbana Champaign, Material Science and Engineering, Champaign, IL 61801, USA. [5]These authors contributed equally: Kaihao Zhang, Mitisha Surana. ✉e-mail: tawfick@illinois.edu

Indeed, most metallic nanocrystalline thin films can accommodate much higher stress than their bulk counterparts due to dimensional constraints on dislocation activities[11,12], thickness-limited microstructure cannot well sustain dislocation pile-ups and leads to limited energy dissipation capability. Therefore, the fracture toughness of an ultrathin metal film is usually tens of times lower than its bulk counterpart[13]. Moreover, the constraint provided by the compliant polymer substrate is only valid for thick metal films, while for ultrathin metal films, racks easily propagate at much smaller strains of just a few percent[8,14]. These catastrophic mechanical failures increase the electrical resistance to several orders of magnitude, severely affecting the functionality and shortening the lifetime of flexible devices.

The failure of electrical interconnects in flexible devices is an electro-mechanical phenomenon. Increase in resistance of metal meshes is related to microcracks. The abrupt increase in electrical resistance of a strained flexible interconnect/electrode is correlated with the onset of unstable crack propagation in materials[9,10,15]. It is crucial to control the crack nucleation and stabilize the crack extension within ultrathin metal films for reliable flexible electronics. Previous studies of high-performance thin metal films have focused on enhancing the metal fracture toughness by solid-solute alloying or deflecting in-plane crack propagation. For example, Kim et al.[16] successfully increased the toughness of a 100 nm thick nanocrystalline Cu film by 38% to ~89 Jm^{-2} by preparing a Cu-Cr thin film nanocomposite with 5 vol.% of Cr inclusions. The weak Cu-Cr interface provides a preferred crack path and thus can effectively deflect the crack propagation and increase the global toughness. Cho et al.[17] showed a configuration with a transferred 2D interlayer such as graphene, molybdenum disulfide, or hexagonal boron nitride between a 200 nm thick Au film and polymer substrate. The buckled crest networks of transferred 2D interlayers can guide the crack propagation in Au film, resulting in intersection and interaction between multiple cracks instead of channel cracks and delay of complete fracture across the entire metal film. However, the above strategies have a limited enhancement in thin metal film's toughness.

In this study, we propose a route to reinforce ultrathin metal film toughness by directly growing graphene onto the metal meshes, which act as catalyst for rapid chemical vapor deposition (CVD) of graphene[18]. This method allows growth of high-quality few-layer graphene (FLG) uniformly on the surface of sub-micron thick photolithographically patterned metal networks without solid-state dewetting defects in addition to removing the need for any post graphene transfer processes. We show that CVD-grown palladium-graphene (PdGr) films exhibit a substantially higher fracture toughness with a low crack nucleation rate and stable crack extension than bare palladium (Pd) films. As a result, CVD-grown PdGr thin film network (TFN) shows higher damage tolerance manifested via a slow increase in electrical resistance even when strained uniaxially to > 60%, while bare Pd networks failed at strains below 40% with an abrupt surge in electrical conductivity. In addition, we carried out systematic fatigue testing for both TFNs in this study. CVD-grown PdGr networks show promise of longer fatigue life than bare Pd ones, especially for thinner films with a large total strain range. With the proposed pre-treatment of in-situ graphene growth, we can easily fabricate ultrathin metallic films with high fracture resistance and high electrical ductility as a stretchable electrode or interconnect, which can accommodate large and cyclic deformations.

Results and discussion
Fabrication and electrical characterization of CVD graphene-metal thin film interconnect

To prepare CVD-grown PdGr nanocomposite interconnect, a photo-lithographically defined Pd network was deposited on a SiO$_2$ (300 nm)/Si substrate by sputtering. This network was directly used as the catalyst for graphene synthesis, as illustrated in Fig. 1a, b. Three thicknesses of Pd substrates 285, 350, and 677 nm were tested in this study. We used a deterministic architecture of the building blocks with horseshoe-shape geometries in a triangular lattice configuration of repeating units (Supplementary Fig. 1a)[19]. We have previously developed a rapid CVD process for high-quality graphene synthesis on ultrathin Pd films without solid-state dewetting[18,20]. Here, as-deposited Pd TFN was first annealed in the He environment at 600 °C for 1 h to release the residual stress from the sputtering process. The annealing step also reduces the grain boundary density (Fig. 1c and Supplementary Fig. 1b, c), which has been previously shown to enable high strain deformation[9]. Additionally in our study, since graphene
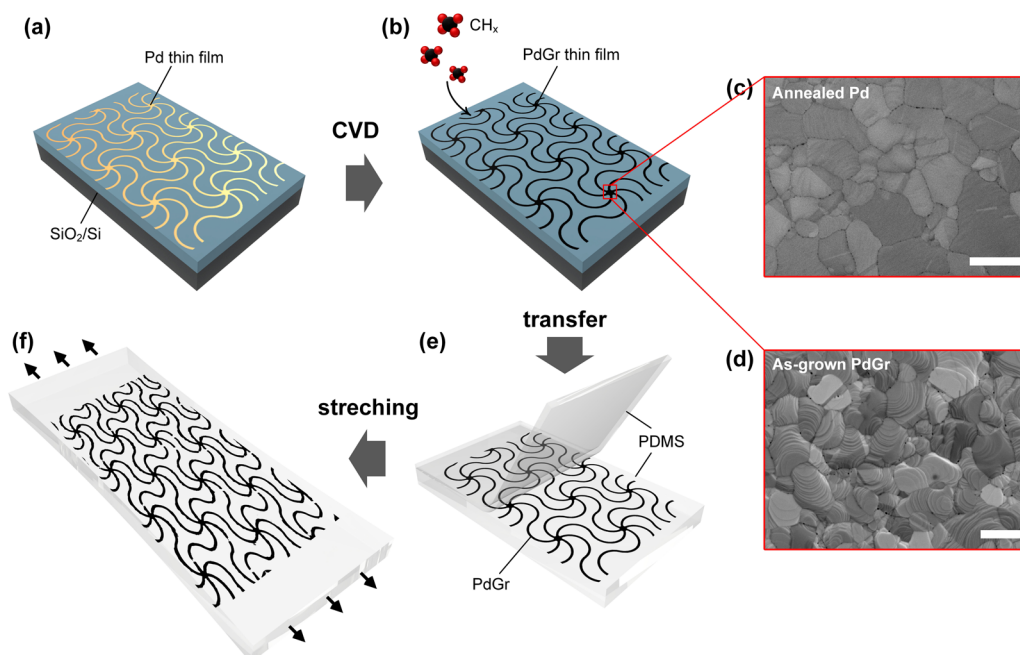
Fig. 1 | Chemical vapor deposition (CVD) of graphene on metal thin film interconnects for stretchable devices. a Schematic of a patterned wavy thin film network (TFN) based on the 'horseshoe' pattern deposited on the SiO$_2$/Si substrate. **b** Schematic of CVD-grown graphene-metal TFN on the SiO$_2$/Si substrate. **c, d** SEM images of annealed Pd and as-grown PdGr thin film surface, respectively, showing the surface morphologies before and after graphene growth. **e** Schematic of CVD-grown PdGr TFN transferred and embedded in a flexible PDMS substrate. **f** Schematic of the deformation of as-fabricated TFN with PDMS carrier under uniaxial tension. Scale bars in (**c, d**): 1 μm.
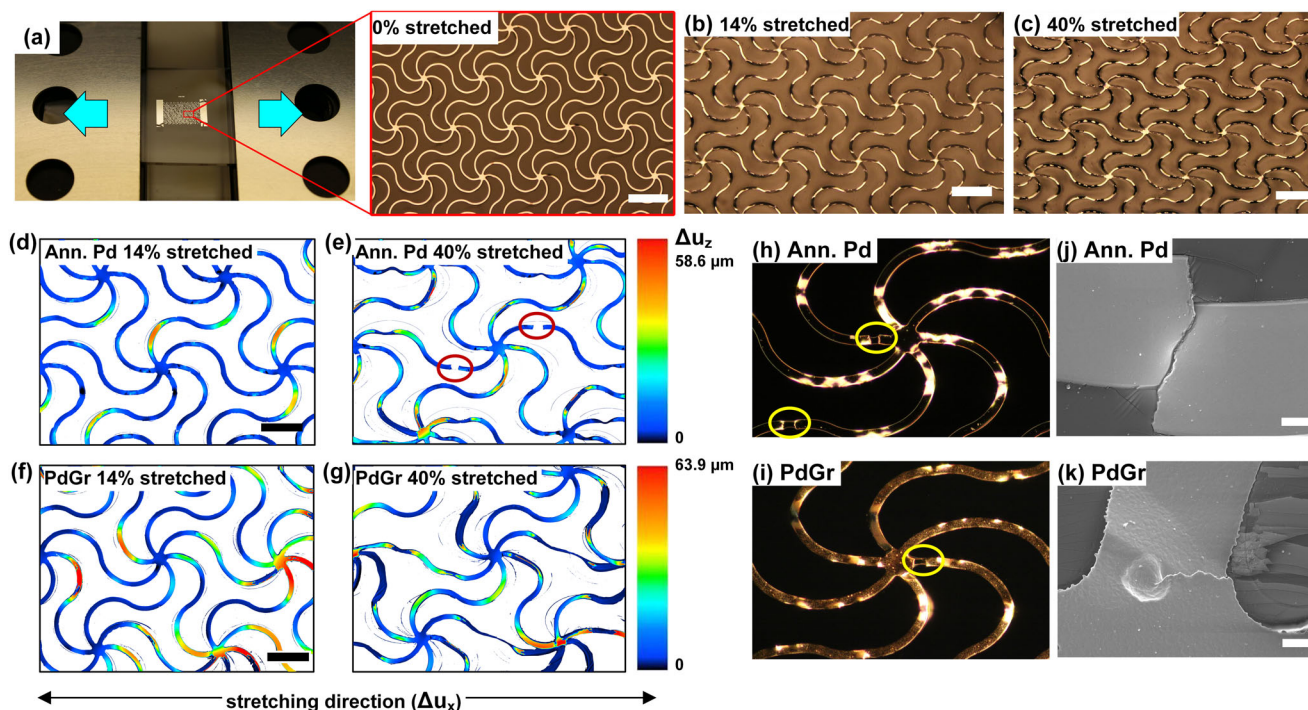
Fig. 2 | Deformation and ligament fracture of patterned TFNs under tensile loading. a Top view OM images of a patterned Pd TFN on a PDMS substrate before tensile loading (stretching). **b, c** Top view OM image of the Pd/PDMS stack under 14 and 40% uniaxial stretching, respectively. **d, e** In-plane and out-of-plane deformation measurements for Pd TFN in PDMS under $\varepsilon = 14$ and 40%. Red circles mark the ligament fractures. **f, g** In-plane and out-of-plane deformation measurements for as-grown PdGr TFN in PDMS under $\varepsilon = 14$ and 40%. **h, i** Dark field OM images of stretched Pd and PdGr ligaments, respectively. Yellow circles highlight the fractured ligaments. **j, k** SEM images of corresponding fracture surfaces of Pd and PdGr TFNs. Scale bars in (**a–c, d, f**): 200 μm, scale bars in (**j, k**): 5 μm.

growth on palladium occurs by carbon precipitation, large Pd grains facilitate uniform graphene synthesis as they enable uniformly distributed carbon dissolution. Supplementary Figure 2a, b present the representative Raman spectra and the G peak location map. Raman analyses indicate that FLG with low defect density fully covers the Pd surface. Supplementary Fig. 2c shows the transmission electron microscope (TEM) images of freestanding PdGr network ligaments verifying the uniform and conformal wrapping of FLG around the Pd. Notably, CVD-grown PdGr exhibits strong graphene-metal interfacial interaction, as graphene is known to have strong affinity to Pd[21–24]. To be specific, Pd-Gr separation distance is 0.25 nm, which is about 24% shorter than that of CVD-grown Cu-Gr[25]. This indicates that the interfacial adhesion energy of Pd-Gr is higher than that of Cu-Gr system ($\sim 12.8\ \mathrm{J\ m^{-2}}$)[26]. Fig. 1d shows the surface morphology of as-grown PdGr, which exhibits surface reconstruction of curved steps and terraces in each grain also indicating strong Pd-Gr adhesion[22,27]. After graphene synthesis, the as-grown PdGr TFN can be transferred and encapsulated inside of a polydimethylsiloxane (PDMS) thin substrate, as illustrated in Fig. 1e, f (See "Methods" for detailed experimental procedures). Liquid metal (Galinstan) was used to connect the TFN to electrodes to avoid connection failure during mechanical deformations.

In general, the electrical conductivity of PdGr TFN is higher than that of annealed Pd by ~10–15%. For example, for 677 nm samples, the PdGr has a conductivity of $10.81 \times 10^6\ \mathrm{S\ m^{-1}}$, compared to the annealed Pd which is $9.50 \times 10^6\ \mathrm{S\ m^{-1}}$, which is a 13.7% increase in electrical conductivity after CVD synthesis. This value varies depending on the number of layers and the thickness of palladium, however a precise trend cannot be established due to the uncertainty in the sputtering and synthesis conditions. This is consistent with our previous studies where we have observed a comparable (~10–15%) increase in electrical conductivity of CVD-grown graphene-metal composite thin film compared to the bare metal thin films[28]. The nickel-multilayer graphene (Ni-MLG) thin films show high electrical conductivity of $9.87 \times 10^6\ \mathrm{S\ m^{-1}}$, which is slightly higher than the annealed Ni film of $9.49 \times 10^6\ \mathrm{S\ m^{-1}}$. The conductivity of the freestanding MLG is

$9.62 \times 10^7\ \mathrm{S\ m^{-1}}$, which is consistent with published values for aligned graphene platelets. Compared to MLG, the few-layer graphene synthesized in the current study have higher crystallinity and uniformity and therefore better electrical conductivity.

Electromechanical resilience under uniaxial tension

We refer to the ability of the network to maintain electrical conductivity as electromechanical resilience. This terminology reflects that it is indeed a coupled mechanical and electrical phenomenon. For instance, an increase in resistance can be correlated with a local mechanical change such as a local crack. We first analyzed the uniaxial deformations in the TFN to study the reinforcing effect of CVD-grown graphene in stretchable electronics. Uniaxial tension was applied to the PDMS-encapsulated TFN using a customized tensile apparatus, as shown in Fig. 2a. Figure 2b, c give representative optical microscope (OM) images of the network under uniaxial stretching with $\varepsilon = 14\%$ and 40%, respectively. At 40% stretching, some cracking occurs, and is responsible for the decrease in TFN's conductance. Hybrid deformations consisting of ligament translation, rotation, twisting, and in- and out-of-plane bending are expected due to the six-fold symmetry of the horseshoe patterns under uniaxial tension. Different contrasts in Fig. 2b, c indicate the out-of-plane ligament buckling due to the small out-of-plane bending stiffness ($\propto wt^3 \approx 3.1 \mu m^4$). However, since the networks are fully embedded in PDMS (10:1), the elastic modulus (~1.3 MPa) of the encapsulating elastomer effectively constrains the out-of-plane deformations[19]. The out-of-plane displacements (Δu_z) of annealed Pd and as-grown PdGr networks in PDMS were measured using a confocal laser scanning microscope during stretching, as shown in Fig. 2d–g. The ratios of out-of-plane to in-plane displacements ($\Delta u_z / \Delta u_x$) for both samples are < 0.012 at $\varepsilon = 40\%$ suggesting that the in-plane bending predominates in the embedded network deformations. For simplicity, we consider the fracture of network ligaments analogous to in-plane fragmentation of thin films in this study. Compared with the brittle type fragmentation of the bare metal thin films, as shown in Fig. 2h, j or previously reported ones with straight channel cracks
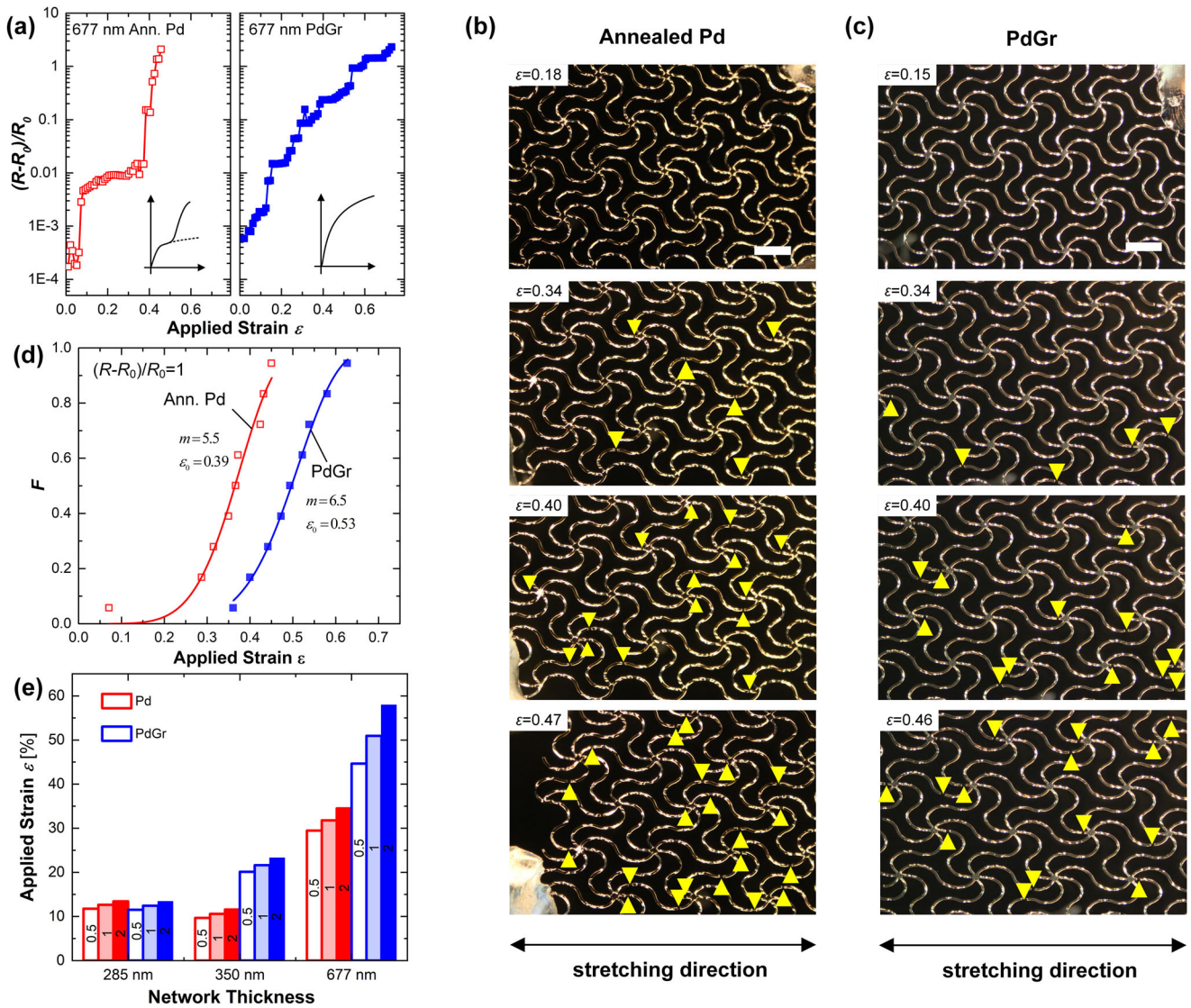
Fig. 3 | Electrofragmentation of patterned TFNs under tensile loading.
a Normalized change of electrical resistance vs. applied strain for Pd and PdGr TFNs.
b, **c** Representative dark-field OM images for Pd and PdGr TFNs under different
tensile strains. Yellow arrows guide the eye to fractured ligaments and ligament
fracture density evolution with applied strain. **d** The Weibull distribution Pd and
PdGr TFNs under uniaxial tension given the criterion for thin film failure set at
$(R - R_0)/R_0 = 1$. **e** Comparison of average applied strains corresponding to $(R - R_0)/R_0 = 0.5$ (hollow), 1 (hatched), and 2 (filled) for Pd (in red) and PdGr (in blue)
TFNs with different film thicknesses. The annotated values in bars indicate
$(R - R_0)/R_0$. Scale bars in (**b**, **c**): 200 μm.

spanning the entire ligament[15,17], PdGr thin film exhibits notable thinning
near the crack and a chisel point-shape fracture surface with serrated
cracking path, (Fig. 2i, k) characteristic of ductile failures in thicker films
and foils.

The primary focus of this study is comparing the results with and
without graphene synthesis for each thickness under different types of
loading. Overall, we focus on the observed reinforcement of CVD-grown
graphene coating in the composite thin films and note that the models and
mechanisms of reinforcement, such as those discussed in the next section,
can be generalized using the thin film electrical conductance degradation
model. A secondary focus of this article is how the thickness of the Pd affects
graphene-induced enhancement. We note that in this case, clear quantita-
tive trends as function of the thickness suffer from uncertainties due to
uncontrolled variations such as material structure variation between dif-
ferent batches of Pd sputtering, and the different growth conditions needed
for each thickness to balance the graphene coverage while avoiding solid
state de-wetting.

It is insightful to observe the rate of increase of the normalized electrical
resistance as a function of strains, to understand the effect of the graphene

growth on thin film electromechanical performance. Figure 3a compares
$(R - R_0)/R_0$ with respect to applied strains. For Pd, the response is marked
by huge jumps in resistivity such as the clear transition at a strain of about
34%, corresponding to the sudden mechanical failure across a large number
of ligaments[15,17]. For $\varepsilon < 34\%$, the resistance increase is mainly from the
strain gauge effect, and thin film ligaments deform to align to the direction of
the applied stress without material fracture. While for $\varepsilon > 34\%$, the resis-
tance exhibits a surge of more than two orders of magnitude with a faster
rate of increase, which is attributed to the abrupt fracture and disconnection
of Pd ligaments. A different $(R - R_0)/R_0$ behavior is observed for PdGr
TFN in Fig. 3a. In general, $(R - R_0)/R_0$ of PdGr increases gradually with
applied strain than that of Pd. Moreover, no abrupt jump in the electrical
resistance is observed. This indicates a stable ligament failure mode in PdGr
TFN. The inset schematics in Fig. 3a illustrate the different electro-
fragmentation modes for Pd and PdGr networks. Notably, PdGr TFN can
accommodate a higher strain than Pd TFN without an abrupt increase in
electrical resistance ($\varepsilon_{Pd} = 46.0\%$ and $\varepsilon_{PdGr} = 73.8\%$ at
$(R - R_0)/R_0 = 2$). Figure 3b, c compare the deformations of Pd and PdGr
networks under an optical microscope and their ligament failures at
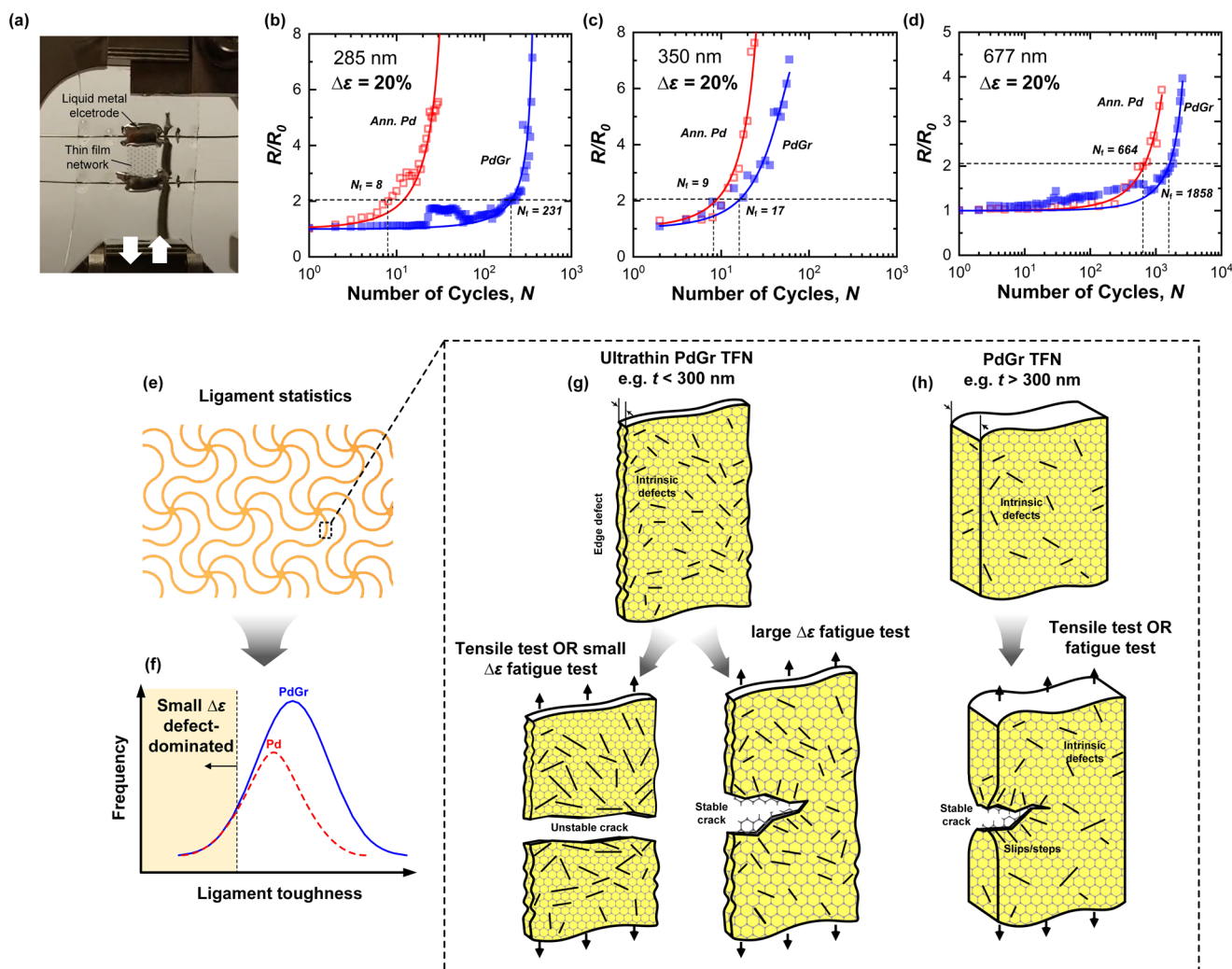
Fig. 4 | Electrical resistance change under fatigue loading. a Photo of the TFN fatigue testing in DMA. **b** Normalized electrical resistance (R/R_0) vs. number of uniaxial tension fatigue cycles for Pd and PdGr films with a thickness of 285 nm and a strain range $\Delta\varepsilon = 20\%$. **c** Film thickness = 350 nm, $\Delta\varepsilon = 20\%$. **d** Film thickness = 677 nm, $\Delta\varepsilon = 20\%$. The solid lines are fittings of the theoretical model for thin film interconnect fatigue behavior[33]. **e, f** Schematics of ligament failure statistics comparing ligament toughness distributions in Pd and PdGr TFNs. **g, h** Schematics of different fracture modes of a ligament in the ultrathin and general as-grown PdGr TFNs during the tensile and fatigue tests.

different applied strains. Yellow arrows guide the reader to the fracture of individual ligaments. Below $\varepsilon = 34\%$, both networks show no ligament failure, while above this threshold, the ligament fracture density in annealed Pd starts increasing rapidly (Fig. 3b). By contrast, the fractures in PdGr are sparse, and the ligament fracture density grows slower and in a more stable manner, see Fig. 3c.

Next, we study the statistics of the electrofragmentation phenomenon. We used the Weibull's weakest link model[29,30] to statistically compare the ligament fracture behaviors in Pd and PdGr networks. Here we defined the electrical failure of thin film interconnect as $(R - R_0)/R_0 = 1$, and according to the model, the probability of network failure exhibits a Weibull distribution as[31]:

$$F(\varepsilon) = 1 - \exp\left[-\left(\frac{\varepsilon}{\varepsilon_0}\right)^m\right] \qquad (1)$$

where m and ε_0 are the Weibull shape and scale parameters which are related to the inverse of deviation and the mean value of the network electrical failure strain. Figure 3d shows the cumulative probabilities of the failure strain for TFN. We obtained the Weibull parameters by fitting to the $F - \varepsilon$ data: $m_{Pd} = 5.5$ vs. $m_{PdGr} = 6.5$ and $\varepsilon_{0_{Pd}} = 0.39$ vs. $\varepsilon_{0_{PdGr}} = 0.53$,

indicating that PdGr is more resistive to tensile damage ($\sim$36% enhancement in the failure strain) and electro-fragmentation occurs in a more stable manner in PdGr networks.

We also measured the network electrical conductivity changes for various films. Figure 3e compares the average applied strains corresponding to $(R - R_0)/R_0 = 0.5$, 1, and 2 for Pd and PdGr TFNs with thickness of 285 nm, 350 nm, and 677 nm. We note that more significant changes in conductivity between the Pd and PdGr for larger thickness, which correspond to larger strains. This point is discussed in more detail in the next section.

Electrical resistance under fatigue loading

Besides quasistatic tensile loading, cyclic stretching was also carried out using a dynamic mechanical analyzer (DMA) under strain range control at a frequency of 2 Hz, as illustrated in Fig. 4a. Figure 4b–d show representative normalized resistance (R/R_0) – loading cycle (N) data for Pd and PdGr films having different thicknesses with a total strain range ($\Delta\varepsilon$) of 20%. We use R/R_0 (which is equal to $1 + (R - R_0)/R_0$) to compare to published studies in the literature. In general, R/R_0 grew slowly when N is low, then experienced an inflection and increased rapidly after a threshold N. The resistance increase is closely associated with the crack formation and propagation in a whole
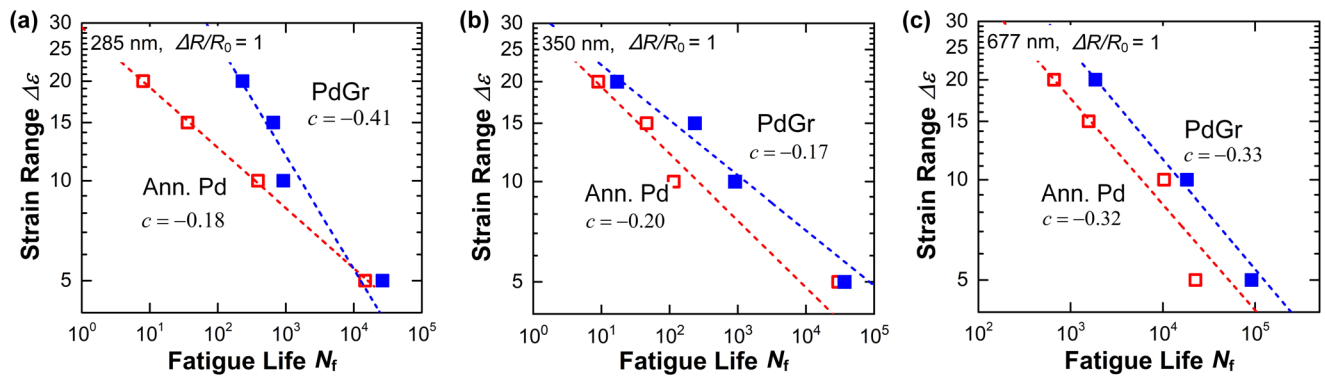
Fig. 5 | Fatigue testing. Applied strain range ($\Delta\varepsilon$) – fatigue life (N_f) correlations for Pd and PdGr TFNs with difference thicknesses: (**a**) 285 nm, (**b**) 350 nm, and (**c**) 677 nm.

thin metal film. In previous studies, $R/R_0 = 1.25$ was selected as thin film fatigue failure criterion, where a crack starts propagating[10,32]. In this context, thin metal films are not continuous but have stretchable wavy patterns. Hence, we used $R/R_0 = 2$ to compare the corresponding fatigue life (N_f) between Pd and PdGr, as marked with dashed lines in Fig. 4b–d. We observed that PdGr TFNs have a 2- to 30-fold longer fatigue life than Pd. Furthermore, we investigated the relation between the electrical failure of ultrathin metal films on compliant substrates to the loss of conductive paths due to cracks initiation and propagation by applying a thin film electrical conductance degradation analytical model[33]. The model bridges the relation between R/R_0 and N as:

$$\frac{R}{R_0} = \left[1 - \frac{wd_g^5}{20}\left(1 - e^{-\left(\frac{\Delta\varepsilon}{t}\right)^k\left(\frac{1}{d_g}\right)N}\right)\right]^{-1} \quad (2)$$

where d_g is the average grain size, which is considered as 500 nm in our experiments, w and k are material constants, $\Delta\varepsilon$ is nominal strain amplitude, and t is film thickness. The term $\Delta\varepsilon/t$ is somewhat intuitive as it represents a measure of the likelihood of damage because it is the deformation to thickness ratio. Notably, the crack nucleation rate is proportional to $(\Delta\varepsilon/t)^k w$ and the extension rate is proportional to $(\Delta\varepsilon/t)^k$[33]. Solid lines in Fig. 4b–d show the least squares fitting results based on $R/R_0 = [1 - A(1 - e^{BN})]^{-1}$ from Eq. 2. Supplementary Table 1 lists the identified fitting parameters A and B. The goodness of fit (R^2) values is close to one, indicating the match between the analytical model and the experimental data. Comparing the $(\Delta\varepsilon/t)^k w$ ($\propto$ crack nucleation rate) and $(\Delta\varepsilon/t)^k$ ($\propto$ crack extension rate) values in Supplementary Table 1, PdGr exhibits prominently lower crack nucleation and extension rates than Pd, especially for thinner networks with large $\Delta\varepsilon$. We attribute this fatigue life enhancement to the high in-plane strength of as-grown high-quality graphene layers and its stronger incorporation with the underlying metal substrate by CVD synthesis.

The electromechanical behavior shown in Fig. 4b–d is a network-level response, governed by the statistical distribution of ligament toughness as shown schematically in Fig. 4e, f. Figure 4g, h illustrate the various toughness behaviors, which govern the individual ligaments. The toughness of the ligaments is affected by defects including microcracks and rough edges formed during fabrication. We expect that the weakest ligaments are dominating the behavior observed in the static tensile tests and in the cyclic fatigue at small strains (< 10%), especially for the thin samples. In this case, graphene does not improve the resistance of these ligaments in this small strain level, which we refer to as defect-dominated regime, shown on the histogram of Fig. 4f. Indeed, Fig. 5a, b show that at the smallest strain level, graphene does not offer any enhancement. Thin TFN, namely 285 nm and 350 nm, possess a considerable number of these defect-dominated ligaments due to fabrication challenges encountered in smaller thickness.

We propose a mechanism whereby defect-dominated ligaments fail pre-maturely during tensile testing or under small strain fatigue loadings, as

intrinsic defects result in unstable cracks which cannot be controlled by the presence of graphene. As a result, we observe negligible strengthening effect of graphene in 285 nm TFNs in Fig. 3e for small strains or in the cyclic tests at small strains (Fig. 4b). On the contrary, under large strain fatigue loadings, for instance in Figs. 4b–, 5a, the response is governed by the mean ligament toughness, i.e., those with the highest frequency according to the schematic of Fig. 4f, as the weakest ligaments have all been already eliminated at small strain. In this case, graphene effectively activates the expected extrinsic toughening mechanisms. We hence believe that the statistics of ligament toughness offer useful insights into understanding the various electro-mechanical measurements of the network.

As the sample thickness is increased, the proportion of defective ligaments decreases, and the defect-dominated regime is no longer observed. In principle, this regime might still be present but at very small strain values which are practically not feasible to study. Hence, for the 677 nm TFN, the effect of graphene improvement of the electromechanical resilience is consistent for all strain levels. However, the magnitude of toughening enhancement is smaller for thicker films due to the smaller surface to volume ratio. This is further discussed in Fig. 6.

Further, we performed a parametric study with networks having different film thicknesses and total strain ranges (5%, 10%, 15%, and 20%), as shown in Supplementary Fig. 3. Generally, the fatigue life of thin film materials subjected to plastic deformation in low-cycle fatigue testing can be correlated with the plastic strain range using the Coffin-Manson relationship[34]:

$$\frac{\Delta\varepsilon_p}{2} \equiv \frac{\Delta\varepsilon}{2} = \varepsilon_f(2N_f)^c \quad (3)$$

where $\Delta\varepsilon_p$ in the original model is the plastic strain range, ε_f and c are the fatigue ductility coefficient and exponent, respectively. Figure 5 summarizes the fatigue testing data and shows the interpretation using Eq. 3. Here we used the nominal total strain $\Delta\varepsilon$ in Eq. 3, and we refer to it as the strain range. The slope in Fig. 5 represents the fatigue ductility exponent (c). For 285 nm thick networks (Fig. 5a), PdGr exhibits a fatigue ductility exponent of -0.41, which is about 2.3 times that of Pd in absolute value. This verifies that CVD-grown PdGr interconnect possesses high resistance to fatigue damages, especially for low-cycle high strain range cyclic loading. However, for thicker films shown in Fig. 5b, c, the fatigue ductility exponents of PdGr and Pd are close to each other and somewhat lower than that of bulk metal materials. It is important to note that the testing of these samples can take up to 2–3 days, which makes it challenging to obtain sufficient repeats. However, the trends are clear, though with some uncertainty due to the lack of repeats. This can be ascribed to several reasons, including (i) thin film failure mode is transferred to transgranular fracture, necking, and de-bonding as film thickness increases[9,10]; (ii) toughening and strengthening effects of CVD-grown FLG become limited to thicker polycrystalline metal substrates when transgranular fracture and necking modes are predominant.
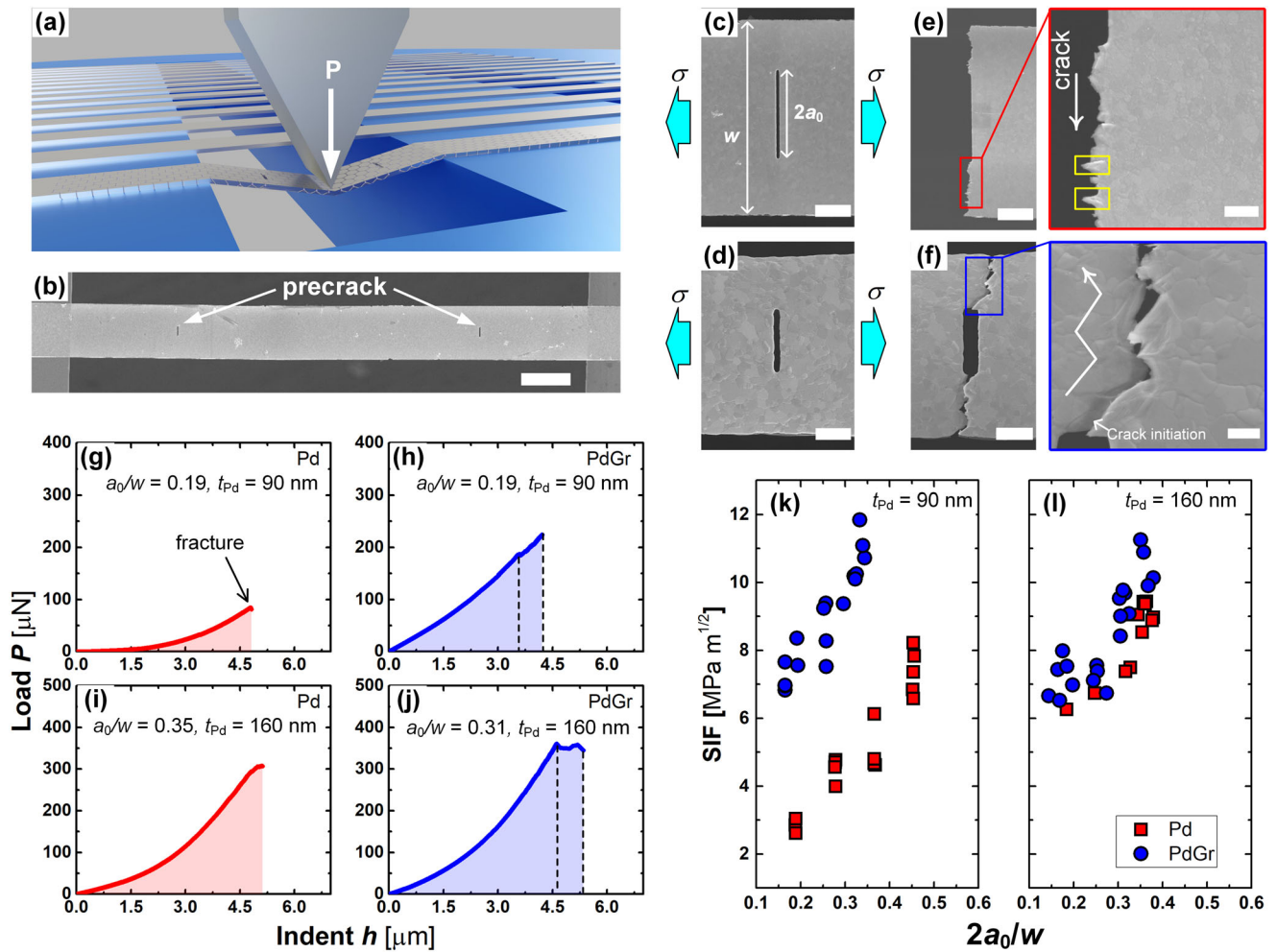
Fig. 6 | Fracture toughness of ultrathin Pd and PdGr ribbons. a Schematic of fracture toughness measurement using a microbridge deflection fracture experiment. **b** Top-view SEM image of a freestanding PdGr nanoribbon with two axial symmetric central notches. **c, d** SEM images of a pre-cracked Pd ribbon (90 nm) before and after fracture. Zoomed-in image shows a relatively straight cracking path with small necking with the comparable size of grains (yellow squares). **e, f** SEM images of a pre-cracked PdGr ribbon (90 nm) before and after fracture. The zoomed-in image highlights the deflected cracking path with chisel point fracture surface and slip lines near the fracture surface. **g, h** the load-indent curves of the Pd and PdGr ribbons with a thickness of 90 nm. **i, j** The load-indent curves of the Pd and PdGr ribbons with a thickness of 160 nm. **k, l** dependence of fracture toughness on ribbon dimension (a_0/w) for Pd and PdGr with different thicknesses. Scale bar in (**b**): 10 μm. Scale bars in (**c–f**): 2 μm, and in the insets: 0.5 μm.

Fracture resistance enhancement by graphene growth

To unveil the underlying mechanisms of PdGr thin films' pronounced resistance to tensile strain and cyclic stretching, we conducted a microbridge deflection fracture experiment to evaluate the thin film fracture toughness[23,35]. As illustrated in Fig. 6a, ultrathin Pd ribbons were transferred over a slotted SiO$_2$/Si substrate so that Pd films became freestanding and doubly clamped. Consequentially, rapid CVD synthesis process was directly applied to these freestanding ultrathin Pd ribbons so that graphene layers fully wrap the freestanding gauge region and pre-existing notch[18,23]. Detailed sample fabrication processes has been published before[23]. To implement the mechanical testing, a wedge indenter applied line loading to the middle of the spanning thin film to create microbridge deflection. Notably, Pd ribbons were doubly clamped to SiO$_2$/Si surface by inter-diffusion in high-temperature CVD processes. Thus, no sliding was observed in the experiments. All freestanding ribbons have a low thickness to length ratio ($t/l < 0.1$), as shown in Fig. 6b, thus the bending stiffness in load (P)-indent (h) relation becomes very small, and the deformation in the ribbon is stretching dominant, especially for deeper indent[35]. As a result, it is reasonable to consider pure tensile testing in two straight ribbon segments. We used focused ion beam to mill two asymmetric central notches for fracture testing. Figure 6c, d show the central notch geometry. Blunt line cracks have

tip radii of <200 nm. In this configuration, we can compute the apparent fracture toughness from the following expression:

$$K_{Ic} = \sigma\sqrt{\pi a_0} \cdot F_I(\alpha) \tag{4}$$

Where σ is the ribbon in-plane stress, $2a_0$ is the length of the pre-existing notches, $F_I(\alpha) = \sqrt{\sec(\alpha\pi/2)}$, and $\alpha = 2a_0/w$, w is the width of the ribbon. We can obtain the ribbon in-plane stress σ by reducing the directly measured indentation load P and indent h by the following:

$$N = \frac{P}{2\sin\theta} \approx \frac{P}{2 \cdot 2h/l_0} \Rightarrow \sigma = \frac{Pl_0}{4hA} \tag{5}$$

Where N is the in-plane force applied to the ribbon, l_0 is the initial length of the ribbon, and A is the cross-sectional area of the ribbon.

The tension applied by indentation triggers mode I fracture in the gauge region with the pre-existing notch. The intrinsic fracture toughness of thin film materials is typically much lower than plane strain fracture toughness (K_{IC}). This is because of many factors, for example, strain localization and the rapid nucleation of cracks with a limited size of the plastic zone. Figure 6e, f present typical morphologies of the fracture surface of bare

Pd and PdGr, respectively. Bare Pd exhibits brittle fracture behavior with a straight cracking path emerging from the pre-existing notch and spanning the rest of the material. By contrast, PdGr ribbon shows a saw tooth-like cracking path with obvious chisel point-shaped necking and a few slip lines near the fracture surface, also see Supplementary Fig. 3. This is indicative of large plastic deformation before failure, and possibly work hardening leading to crack deflection. The interesting and periodic crack patterns have previously been observed in cracking of a thin film attached to the substrate[36], which is a similar effect of the presence of the graphene coating around the thin Pd. The serrated crack morphology is often observed when significant ductile behavior is present during crack propagation. The initiated crack follows the direction of the maximum shear stress, which is an orientation of 45° due to the plane stress nature in thin films. However, if the crack propagation is stable and the material is ductile, significant work hardening takes place in the material ahead of the crack tip. This can redirect the cracking path from +45° to −45° following the other maximum shear stress direction[20]. Here the actual cracking path is more complicated than the neat 45° zigzag shape due to the polycrystalline texture of Pd films used in this study. Figure 6g–j show the corresponding *P-h* curves for Pd and PdGr with two different thicknesses. Notably, Pd ribbons failed instantly after P reaches the breaking load P_b where the crack propagated straight through the material. PdGr ribbons exhibit higher breaking loads and maximum indents than Pd ones. More importantly, remarkable work hardening effect was observed in PdGr (areas between two dashed lines in Fig. 6h, j). The thinner PdGr ($t_{Pd} = 90 nm$) shows the higher increase in fracture energy (the blue enveloped areas in Fig. 6h, j compared with the red areas in Fig. 6g, i) to Pd than the thicker ones ($t_{Pd} = 160 nm$). As a result, thin film fracture toughness can be estimated using Eq. 4, and $K_{Ic}(PdGr)$ is about 2.7 times of $K_{Ic}(Pd)$ for ribbons with $t_{Pd} = 90 nm$ (Fig. 6k). This toughening effect is also promising when compared with other thin metal films like copper[37] and aluminum[38]. Notably, as film thickness increases, $K_{Ic}(Pd)$ rises and becomes close to $K_{Ic}(PdGr)$, as shown in Fig. 6l. We attribute this size-dependent graphene toughening effect to the effective surface dislocation/extrusion suppression by conformal graphene growth on ultrathin metal films with a limited plastic zone.

On the material level, the toughening mechanisms may be different for various thicknesses. For thicknesses < 300 nm, intergranular fracture can be the dominant failure mode because thickness constraints suppress the yield zone size. Figure 6e and Supplementary Fig. 4c also depict the intergranular fracture surfaces under large tensile strain. Graphene activates several toughening mechanisms both intrinsically and extrinsically. Intrinsically, graphene increases the size of the yielding zone due to its high stiffness and large strain to failure, while extrinsically, it causes grain bridging. These mechanisms deflect the crack path forming a serrated fracture surface, as shown in Fig. 6f and Supplementary Fig. 4a, b.

For thickness > 600 nm, we observe local necking and cold working as shown in Supplementary Fig. 4e, f, which indicate the presence of intrinsic toughening mechanisms. These films show a longer fatigue life than 285 nm Pd films (see Fig. 4b–d or compare the crack nucleation rate and extension rate in Supplementary Table 1). The presence of graphene increases the fatigue life due to extrinsic toughening, though by a more limited amount due to the smaller surface to volume ratio.

In summary, we demonstrated a strategy of using CVD synthesis of graphene conformally wrapping thin film meshes to improve the electromechanical stability and fatigue life of ultra thin flexible interconnects upon large deformations and cyclic loading. High-quality uniform graphene coating and its intimate interface with underlying metal films significantly lower the crack nucleation and the crack extension rates and introduce considerable work hardening ahead of the crack tip thus deflecting the crack propagation direction and leading to serrated chisel point-shape fracture surface with a number of slip lines near the fracture surface. As a result, graphene growth effectively enhances the interconnect fracture toughness (e.g., ~36% enhancement in the failure strain) and fatigue life (e.g., 2 ~ 30-fold longer fatigue life). We carried out quasistatic electro-fragmentation experiments and electrical conductivity fatigue testing on PDMS-encapsulated Pd and PdGr TFNs with various film thicknesses and total strain ranges. The results show the superior electromechanical performance of PdGr networks over the Pd samples under large uniaxial tension beyond 60% and repeated stretching with a strain range of up to 20%. Microbridge deflection fracture experiments were also implemented to evaluate the fracture toughness of Pd films before and after graphene growth. PdGr films exhibit about 2.7 times higher fracture toughness than bare Pd. Moreover, this toughening effect is more prominent for thinner Pd films. The proposed CVD graphene coating approach paves the way to harness graphene-metal nanocomposite materials to improve the robustness of stretchable thin film electronics.

Methods

CVD growth of graphene onto metal thin films

Pd TFNs having horseshoe-shape geometries with three thicknesses of 285, 350, and 677 nm were sputtered on to SiO_2 (300 nm)/Si substrates. The as-deposited Pd TFNs were annealed in the He environment at 600 °C for 1 h. We directly used the annealed Pd TFNs as the metal catalyst for chemical vapor deposition of graphene: a tube furnace was heated to 1100 °C with flowing of He (100 sccm), when furnace temperature stabilized at 1100 °C, CH_4 (50 sccm) was introduced, then Pd TFN sample was quickly inserted into the hot zone using a transfer arm for synthesis. Synthesis time are 10 s for 285 nm Pd, 15 s for 350 nm Pd, and 30 s for 677 nm Pd. During growth, the vacuum is maintained at 1.72 Torr. After synthesis, the TFN sample was rapidly retracted out of the hot zone for natural cooling while maintaining controlled flow of CH_4 and He gases.

To accommodate the high-temperature instability of Pd films due to solid state de-wetting, we shorten the CVD synthesis period for thinner films. It is important to note that the cooling rate is the main factor controlling the number of layers of graphene in segregation growth, and this has been kept nearly constant. Hence, although different graphene growth time was adopted, as-grown graphene layer on different Pd TFNs exhibit the same thickness of ~0.7–1 nm. We suspect that due to the different duration, while the graphene thickness is the same, the coverage uniformity may be less optimal especially for thinner films like the 285 nm Pd films.

Fabrication of graphene-metal thin film interconnect

The annealed Pd or the CVD-grown PdGr TFNs can be covered with a thin PMMA protection layer by spin coating and baking (90 °C, 90 s). The PMMA/TFNs/SiO_2/Si stack was soaked in a 0.3 vol.% HF solution for ~10 s then carefully merged into DI water. The PMMA/TFNs can easily delaminate from the SiO_2/Si substrate and float on the water. We then delaminated the PMMA/TFNs onto a PDMS (Sylgard 184, 10:1) substrate using the wedge transferring method. Notably, the PDMS substrate is semi cross-linked by curing at room temperature for less than 12 h. After air drying, the PMMA protection layer was removed with Acetone. Liquid metal (Galinstan) was used to bond the TFNs to electrodes. The whole electronics was finally encapsulated by depositing another layer of PDMS on the top and curing in an oven at 70 °C for 4 h.

Material characterization and electromechanical behaviors testing

The morphology and microstructures of the stretchable TFNs were studied using an optical microscope (Zeiss AXIO), a laser scanning microscope (Keyence VK-X1000), a scanning electron microscope (SEM, JEOL 7000 F), and a high-resolution transmission electron microscope (TEM, JEOL 2100 Cryo). Graphene coverage and crystallinity were characterized using a high-resolution Raman spectroscopy imaging system (Horiba LabRAM HR, with a 405 nm laser wavelength). Electrical conductivity degradation tests were carried out using a digital multimeter (Keysight 34465 A), in situ, under an optical microscope with an in-house made tensile apparatus that enables recording the network's electrical resistance during static uniaxial stretching. For electromechanical robustness characterization under fatigue loadings, a dynamic mechanical analyzer (DMA, TA850) and a digital multimeter were used for electrical conductivity fatigue testing. A

nanoindenter (Hysitron TI-950) with a wedge probe (200 ± 50 nm tip radius, 15 µm edge, 30° defining angle, Micro Star Tech.) was used for mechanical fracture testing with a microbridge testing configuration.

Data availability

References

1. Rogers, J. A., Someya, T. & Huang, Y. Materials and Mechanics for Stretchable Electronics. *Science* **327**, 1603–1607 (2010).
2. Lu, N. & Kim, D.-H. Flexible and stretchable electronics paving the way for soft robotics. *Soft Robot.* **1**, 53–62 (2014).
3. Kappassov, Z., Corrales, J.-A. & Perdereau, V. Tactile sensing in dexterous robot hands — Review. *Robot. Auton. Syst.* **74**, 195–220 (2015).
4. Bowden, N., Brittain, S., Evans, A. G., Hutchinson, J. W. & Whitesides, G. M. Spontaneous formation of ordered structures in thin films of metals supported on an elastomeric polymer. *Nature* **393**, 146–149 (1998).
5. Kim, D.-H. et al. Epidermal electronics. *Science* **333**, 838–843 (2011).
6. Xu, S. et al. Assembly of micro/nanomaterials into complex, three-dimensional architectures by compressive buckling. *Science* **347**, 154–159 (2015).
7. Huang, Y. et al. Assembly and applications of 3D conformal electronics on curvilinear surfaces. *Mater. Horiz.* **6**, 642–683 (2019).
8. Lu, N., Wang, X., Suo, Z. & Vlassak, J. Metal films on polymer substrates stretched beyond 50%. *Appl. Phys. Lett.* **91**, 221909 (2007).
9. Lu, N., Suo, Z. & Vlassak, J. J. The effect of film thickness on the failure strain of polymer-supported metal films. *Acta Mater.* **58**, 1679–1687 (2010).
10. Sim, G.-D., Lee, Y.-S., Lee, S.-B. & Vlassak, J. J. Effects of stretching and cycling on the fatigue behavior of polymer-supported Ag thin films. *Mater. Sci. Eng.: A* **575**, 86–93 (2013).
11. Arzt, E. Size effects in materials due to microstructural and dimensional constraints: a comparative review. *Acta Mater.* **46**, 5611–5626 (1998).
12. Haque, M. A. & Saif, M. T. A. Strain gradient effect in nanoscale thin films. *Acta Mater.* **51**, 3053–3061 (2003).
13. Preiß, E. I., Merle, B. & Göken, M. Understanding the extremely low fracture toughness of freestanding gold thin films by in-situ bulge testing in an AFM. *Mater. Sci. Eng.: A* **691**, 218–225 (2017).
14. Baëtens, T., Pallecchi, E., Thomy, V. & Arscott, S. Cracking effects in squashable and stretchable thin metal films on PDMS for flexible microsystems and electronics. *Sci. Rep.* **8**, 9492 (2018).
15. Leterrier, Y., Pinyol, A., Rougier, L., Waller, J. H. & Månson, J.-A. E. Electrofragmentation modeling of conductive coatings on polymer substrates. *J. Appl. Phys.* **106**, 113508 (2009).
16. Kim, H.-G., Yi, J.-W., Kim, S.-W., Kim, K.-S., & Shravan, K. K. Fracture toughness of free-standing nanocrystalline copper–chromium composite thin films. *Acta Mater.* **84**, 95–109 (2015).
17. Cho, C. et al. Strain-resilient electrical functionality in thin-film metal electrodes using two-dimensional interlayers. *Nat. Electron.* 1–8 https://doi.org/10.1038/s41928-021-00538-4 (2021).
18. Zhang, K., Androulidakis, C., Chen, M. & Tawfick, S. Gilding with graphene: rapid chemical vapor deposition synthesis of graphene on thin metal leaves. *Adv. Funct. Mater.* **28**, 1804068 (2018).
19. Jang, K.-I. et al. Soft network composite materials with deterministic and bio-inspired designs. *Nat. Commun.* **6**, 6566 (2015).
20. Zhang, K. & Tawfick, S. Graphene Synthesis on Ultrathin Metal Catalyst Films. in *Volume 2: Processes; Materials* V002T04A009. https://doi.org/10.1115/MSEC2019-2992 (American Society of Mechanical Engineers, Erie, Pennsylvania, USA, 2019).
21. Giovannetti, G. et al. Doping graphene with metal contacts. *Phys. Rev. Lett.* **101**, 026803 (2008).
22. Yi, D. et al. What drives metal-surface step bunching in graphene chemical vapor deposition? *Phys. Rev. Lett.* **120**, 246101 (2018).
23. Zhang, K., Surana, M., Haasch, R. & Tawfick, S. Elastic modulus scaling in graphene-metal composite nanoribbons. *J. Phys. D: Appl. Phys.* **53**, 185305 (2020).
24. Ananthakrishnan, G. et al. Graphene-mediated stabilization of surface facets on metal substrates. *J. Appl. Phys.* **130**, 165302 (2021).
25. Wang, Q. J. & Che, J. G. Origins of distinctly different behaviors of Pd and Pt contacts on graphene. *Phys. Rev. Lett.* **103**, 066802 (2009).
26. Das, S., Lahiri, D., Lee, D.-Y., Agarwal, A. & Choi, W. Measurements of the adhesion energy of graphene to metallic substrates. *Carbon* **59**, 121–129 (2013).
27. Surana, M. et al. Strain-driven faceting of graphene-catalyst interfaces. *Nano Lett.* **23**, 1659–1665 (2023).
28. Zhang, K., Poss, M., Chen, P.-J. & Tawfick, S. Strengthening nickel by in situ graphene synthesis. *Adv. Eng. Mater.* **19**, 1700475 (2017).
29. Weibull, W. A Statistical Theory of the Strength of Materials. *Proc Roy Swed Inst Eng Res* **151**: 5−45 (1939).
30. Tavares da Costa, M. V., Bolinsson, J., Neagu, R. C., Fayet, P. & Gamstedt, E. K. Experimental assessment of micromechanical models for fragmentation analysis of thin metal oxide coatings on polymer films under uniaxial tensile deformation. *Surf. Coat. Technol.* **370**, 374–383 (2019).
31. Meyers, M. & Chawla, K. *Mechanical Behavior of Materials*, 2nd Edn. (Cambridge University Press, Cambridge, New York, 2009).
32. Sim, G.-D., Won, S. & Lee, S.-B. Tensile and fatigue behaviors of printed Ag thin films on flexible substrates. *Appl. Phys. Lett.* **101**, 191907 (2012).
33. Cheng, J. & Li, Z. An electrical resistance degradation model for thin film under fatigue loading. *Fatigue Fract. Eng. M.* **43**, 2582–2596 (2020).
34. Suresh, S. *Fatigue of Materials*, 2nd Edn. (Cambridge University Press, Cambridge, New York, 1998).
35. Espinosa, H. D. & Bei Peng. A new methodology to investigate fracture toughness of freestanding MEMS and advanced materials in thin film form. *J. Microelectromech. Syst.* **14**, 153–159 (2005).
36. Marthelot, J. et al. Self-replicating cracks: a collaborative fracture mode in thin films. *Phys. Rev. Lett.* **113**, 085502 (2014).
37. Hirakata, H. et al. Size effect on fracture toughness of freestanding copper nano-films. *Mater. Sci. Eng.: A* **528**, 8120–8127 (2011).
38. Haque, M. A. & Saif, M. T. A. In situ tensile testing of nanoscale freestanding thin films inside a transmission electron microscope. *J. Mater. Res.* **20**, 1769–1777 (2005).

Acknowledgements

Author contributions

K. Zhang, M. Surana, and S. Tawfick conceived of the research topic. K. Zhang, M. Surana and J. Yaacoub conducted the experiments. K. Zhang conducted the theoretical analyses. All authors analyzed the data, discussed the results, and reviewed the manuscript.

Competing interests

The authors declare no competing interests.

Additional information

Supplementary information The online version contains
Supplementary Material available at
https://doi.org/10.1038/s41528-024-00300-8.

Correspondence and requests for materials should be addressed to
Sameh Tawfick.

Reprints and permissions information is available at
http://www.nature.com/reprints

Publisher's note Springer Nature remains neutral with regard to
jurisdictional claims in published maps and institutional affiliations.